Sensor and Simulation Notes

Note 476

16 June 2003

Analysis of an Offset Impulse-Radiating Antenna

Kangwook Kim and Waymond R. Scott, Jr.

School of Electrical and Computer Engineering

Georgia Institute of Technology

ABSTRACT

Two offset IRAs are numerically modeled and analyzed. The reflector of the offset IRA is an offset portion of a paraboloid that is carved out by the intersection of the paraboloid and a cone whose apex is at the focal point of the paraboloid. A pair of conical curved plates is placed on the surface of the cone as TEM feed arms. The TEM feed arm of the first IRA is conical throughout its length and terminated at the reflector through two electrically small resistors. The TEM feed arm of the second IRA is partly conical and tapered to one electrically small resistor. The second IRA performs better in terms of the reflected voltage in the transmission line. The second IRA is further analyzed and compared with a center-fed IRA. The radiated waveforms both in the far- and near-zones, radiation patterns, impulse and prepulse amplitude distributions as functions of observation angle, spot sizes, and power budgets for the offset IRA and the center-fed IRA are presented and compared. The results show that the tail waveform of the offset IRA is significantly lower in amplitude and simpler in shape than that of the center-fed IRA. Both IRAs have a shadow behind the reflector; the shadow location of the offset IRA may be useful in bistatic radar applications.

I. Introduction

A variety of applications, such as ultra-wideband weapons and remote sensing, require an antenna that radiates a temporally short electromagnetic pulse [1–5]. One candidate for such applications is the reflector-type impulse-radiating antenna (IRA), which is a parabolic reflector fed by a conical transverse electromagnetic (TEM) structure whose apex is located at the focal point of the reflector [6–9]. Typically, the reflector is a circular portion of a paraboloid around the vertex, and the TEM feed structure is symmetric with respect to the rotational axis of the paraboloid (center-fed IRA).

The TEM feed structure guides the spherical TEM wave launched at the apex. Then, the reflector scatters the TEM wave to form an aperture, which is focused at infinity on the rotational axis of the reflector. Because the TEM feed structure is centered in the path of the reflector-scattered wave, it blocks the aperture [10, 11]. This blockage causes, first, the reduction in the impulse amplitude and, second, multiple reflections inside the antenna. The multiple reflections cause ripples in the tail of the radiated waveform, which is an undesired characteristic especially in remote sensing applications.

One method of reducing the blockage is reducing the size of the TEM feed structure. However, this leads to the increase in the characteristic impedance of the TEM feed structure, making it difficult to match the antenna to the source [12]. Another method is using an offset geometry [13,14]. In this geometry, a different portion of the paraboloid is used as a reflector, and the symmetry line of the TEM feed structure is appropriately tilted away from the rotational axis of the paraboloid. With an appropriate selection of a paraboloidal portion as the reflector, the TEM feed structure can be removed from the path of the reflector-scattered wave, and therefore the blockage can be minimized. Thus, it is worthwhile investigating the characteristics of the IRA with an offset geometry (offset IRA).

In this paper, we analyze the offset IRA with a numerical model. The numerical model is developed using the method of moments code in the EIGER code suite [15, 16]. The performance of the numerical model using EIGER has been validated in [17]. Two offset IRAs with different TEM feed arm terminations are modeled. For one IRA, each TEM feed arm is terminated at the reflector with two resistors. For the other IRA, each

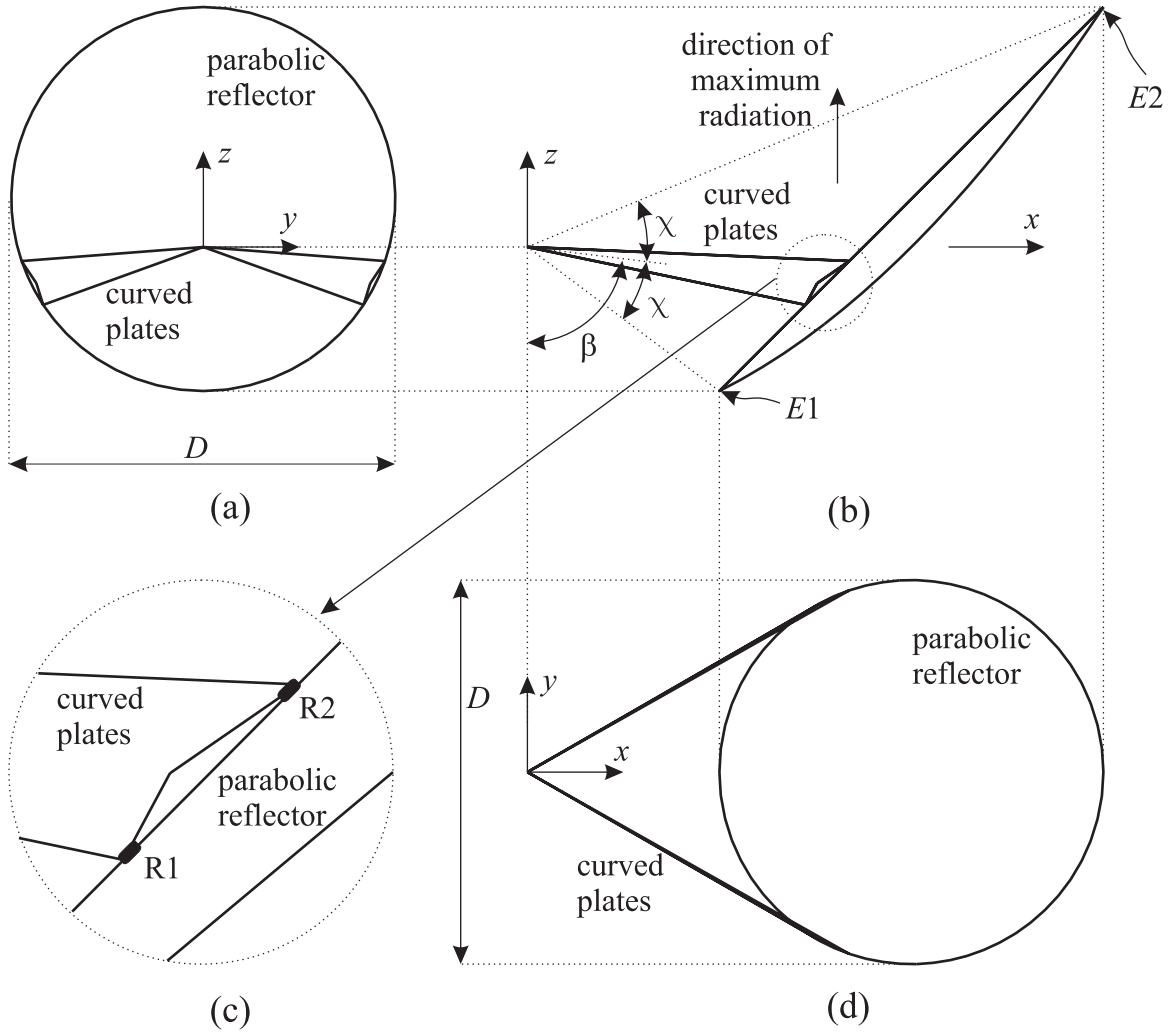

Fig. 1. Geometry of the offset IRA. (a) Projection onto the y-z plane. (b) Projection onto the x-z plane. (d) Projection onto the x-y plane. (c) Magnification of the region around the feed arm termination.

TEM feed arm is tapered and terminated at the reflector with one resistor. It is shown that the reflected voltage in the transmission line can be lowered more with the termination scheme used for the second IRA. The second IRA is further analyzed and compared with a center-fed IRA.

II. Model I: Two-Resistor Feed Arm Termination

Consider the geometry shown in Fig. 1. The reflector is a portion of a paraboloid

that is carved out by the intersection of the paraboloid and a cone. The equation of the paraboloid in the rectangular coordinate system is

$$x^2 + y^2 = 4F(z + F), \tag{1}$$

where F is the focal length of the paraboloid. The paraboloid is rotationally symmetric with respect to the z-axis and has the focus at the coordinate origin. The equation of the cone is

$$\sqrt{(x\cos\beta + z\sin\beta)^2 + y^2} = (x\sin\beta - z\cos\beta)\tan\chi, \tag{2}$$

where χ is the interior half angle of the cone, and β is the angle that the rotational axis of the cone makes with the z-axis in the x-z plane. The intersection of the two surfaces is an ellipse and its projection onto the x-y plane is a circle of diameter $D = 2F$ [18]. Thus, when the reflector is fed a spherical TEM wave launched at the coordinate origin, the reflector forms an aperture of radius D, which is focused at infinity on the z-axis.

To guide the spherical TEM wave to the reflector, a pair of curved plates [12, 19] is used. Curved plates cause significant aperture blockage in the center-fed geometry. However, in an offset geometry, they have an advantage over other frequently considered TEM feed arms because they can be made to cause almost no blockage. The curved plates are placed on the surface of the cone such that they form a spherical TEM transmission line with the characteristic impedance of 400Ω.

Each plate is connected to the reflector through two electrically small resistors ($R1$, $R2$), e.g., chip resistors, which improve the input impedance of the antenna at low frequencies. The parallel resistance of the two resistors at each plate is kept at 200Ω, so the series resistance of one pair of the TEM feed arms at zero frequency is 400Ω. The resistances of the two resistors may be adjusted, while the parallel resistance is kept at 200Ω, in an attempt to reduce the reflected voltage in the transmission line which is connected to the TEM feed arms.

The offset IRA in Fig. 1 has reflection symmetry with respect to the x-z plane. Thus, half of the geometry can be replaced with a perfect electric conductor (PEC) plane in the numerical model to improve the efficiency. The efficiency of the model can be further improved by using a different mesh for each frequency, i.e., using a coarser mesh for a lower

frequency and a denser mesh for a higher frequency. In this paper, two meshes are used to calculate the responses of the offset IRA at 150 equally spaced points within a normalized frequency range of $D/\lambda = 0.102$ to $D/\lambda = 15.3$.[1] The mesh for the lower 75 frequencies contains 5590 triangle elements, and the mesh for the higher 75 frequencies contains 11091 triangle elements.

The electrically small resistors are modeled using a delta-gap lumped impedance model. The mesh is excited by a delta-gap voltage source placed at the apex of the TEM feed arms. The electric field integral equation with linear basis functions is used to solve for the mesh currents. The calculation was conducted by running the EIGER physics solver (EIGER Solve) on the Beowulf cluster at the Electromagnetics/Acoustics Laboratory at the Georgia Institute of Technology. The total run time for the mesh current calculation was approximately 86.1 hours using 32 computer nodes; each node is equipped with an AMD Athlon$^{\text{TM}}$ 2200+ processor. The electric field and input impedance can then be obtained by running the EIGER physics solver for secondary quantities (EIGER Analyze).

The results obtained from EIGER are those for half of the IRA. The responses of the whole IRA can be obtained by halving the currents and fields and doubling the input impedance of the half IRA. The responses in the frequency domain are then transformed into the time domain for a voltage pulse incident in a 400Ω transmission line, which is matched to the TEM feed arms. The input pulses considered in this paper are a step-like and a Gaussian. These functions are defined as follows:

$$\text{Step-like:} \quad V(t) = V_0 \left\{ \frac{1}{2} + \frac{1}{2} \operatorname{erf}\left(k_1 \frac{t}{t_{10\text{-}90\%}} \right) \right\}, \tag{3}$$

$$k_1 = 2 \operatorname{erf}^{-1}(0.8) \simeq 1.8124,$$

$$\text{Gaussian:} \quad V(t) = V_0 e^{-\ln 16 (t/t_{FWHM})^2}. \tag{4}$$

Here, $\operatorname{erf}(t)$ is the error function, and the pulse parameters $t_{10\text{-}90\%}$ and t_{FWHM} are the 10% –

[1]Note that the upper frequency limit was chosen because of computer run time considerations, not limits on the IRA. The chosen upper frequency limit gives us reasonable run times while giving us enough frequency content to see essentially all of the interesting interactions in the antennas. This upper frequency limit sets the minimum pulse parameters in the later graphs.

90% rise time of the step-like pulse and the full-width half-maximum of the Gaussian pulse, respectively [20]. The waveforms and their frequency spectrums are shown in [17].

In Fig. 2, the waveforms of the reflected voltages in the transmission line (V_{refl}/V_0) are graphed for three IRAs with the termination resistors $(R1, R2) = (400\Omega, 400\Omega)$, $(600\Omega, 300\Omega)$, and $(1000\Omega, 250\Omega)$, whose parallel resistances are all 200Ω. The antenna is driven by a step-like pulse with $t_{10\text{-}90\%}/\tau_a = 0.1$ and a Gaussian pulse with $t_{FWHM}/\tau_a = 0.1$, where $\tau_a = D/c$ is the time required by light to travel the length of the aperture diameter. The first reflection seen at $t/\tau_a \simeq 0$ comes from the junction between the transmission line and the antenna (apex of the cone). This reflection is due to the approximation made to the apex geometry (Fig. 5 (a)). The first possible disturbance after this reflection is the signal from the edge of the reflector, which appears at $t/\tau_a \simeq 1.25$. However, the waveform is not exactly zero over the time interval $0 < t/\tau_a < 1.25$. This is due to a small error in the characteristic impedance of the TEM feed arms predicted by the numerical model (1%).

In the figure, T_{E1} and T_{E2} mark the first possible signals from the closest and the farthest points on the reflector from the apex. T_{R1} and T_{R2} mark the first possible signals from the resistors. In Fig. 2 (b), the signal T_{R1} is negative and the signal T_{R2} is positive. This means the signal T_{R1} is a reflection from lower impedance, and the signal T_{R2} is a reflection from higher impedance. Thus, one would think the reflected voltage would be lowered by increasing $R1$ and decreasing $R2$. The figure shows that the amplitude of the signal T_{R2} is lowered with decreasing $R2$. However, the amplitude of the signal T_{R1} is hardly changed. In fact, the reflected voltage over the interval between T_{E1} and T_{R1} cannot be lowered by adjusting $R1$ and $R2$ because the signal in the interval is due to the reflection from lower part of the reflector, which is closer to the apex than the resistors are.

One way to lower the signal over the interval between T_{E1} and T_{R1} may be tapering the TEM feed arms appropriately. This results in gradually increasing impedance along the tapered section and therefore causes positive reflection [21]. This positive reflection can compensate for the negative reflection over the interval between T_{E1} and T_{R1}. In the next section, the TEM feed arm is tapered in an attempt to lower the reflected voltage.

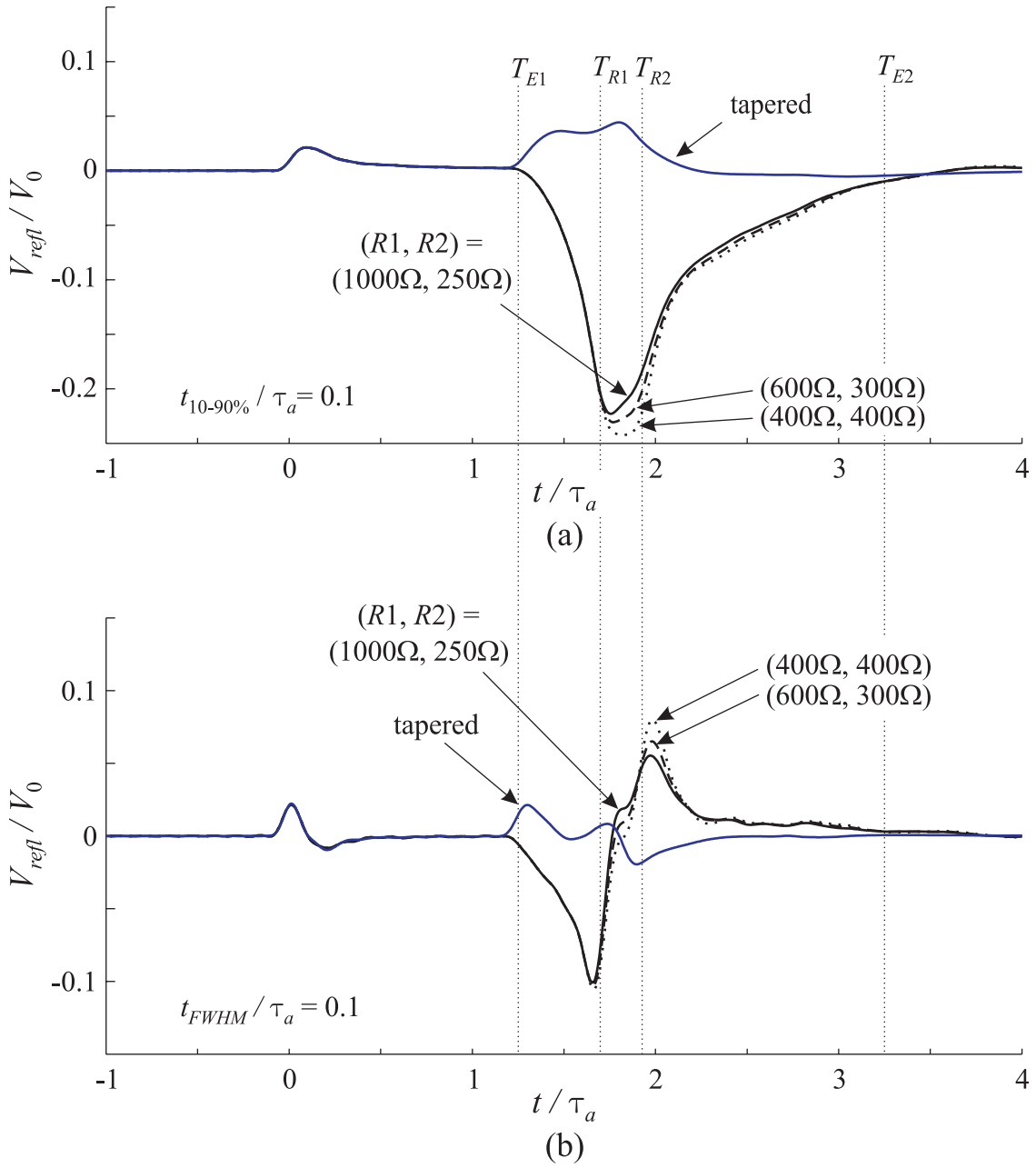

Fig. 2. Reflected voltages in the transmission line for the offset IRAs with the Model I geometry and the offset IRA with the Model II geometry. In the Model I geometry, each TEM feed arm is terminated with two resistors: $(R1, R2) = (400\Omega, 400\Omega)$, $(600\Omega, 300\Omega)$, and $(1000\Omega, 250\Omega)$. In the Model II geometry, the TEM feed arm is tapered and terminated with one resistor. The input pulses for the graphs are (a) a step-like pulse with $t_{10\text{-}90\%}/\tau_a = 0.1$ and (b) a Gaussian pulse with $t_{FWHM}/\tau_a = 0.1$.

III. Model II: Tapered Feed Arm Termination

Consider the tapered TEM feed arms shown in Fig. 3. The TEM feed arms are conical within a sphere of radius L centered at the apex, where a spherical TEM wave launched at the apex propagates outwardly without disturbance. Outside the spherical region, each TEM feed arm is tapered and terminated with a small resistor. When the TEM feed arms are projected onto a plane normal to the cone axis, they can be described by an interior angle $\alpha(r)$:

$$\alpha(r) = \begin{cases} \alpha_0, & 0 < r \leq L, \\ \alpha_0 + g(r), & L < r < L_A, \end{cases} \tag{5}$$

where L_A is the total length of a TEM feed arm, and $g(r)$ is the description of the taper. Here, α_0 is chosen to be 16.3° to make the characteristic impedance of the undisturbed region 400Ω. L is set equal to the distance from the apex to the closest point on the reflector. This causes a positive signal from the taper to appear in the reflected voltage waveform from T_{E1}. For the taper, a simple linear taper is chosen, e.g.,

$$g(r) = \frac{r - L}{L_A - L}(\alpha_{min} - \alpha_0), \tag{6}$$

where $\alpha_{min} = 0.160^\circ$ is the angle made by the small resistor.

The reflection from this TEM feed arm can be estimated by a simple model, which assumes that only a TEM mode exists along the entire TEM feed arm, and that the TEM feed arm is perfectly terminated by a 400Ω load. In the simple model, the characteristic impedance of the incremental section between radii r and $r + \Delta r$ can be obtained from

$$Z_c(r) = \eta_0 \frac{K(m(r))}{K(1 - m(r))}, \quad m(r) = \left[\frac{1 - \sin(\alpha(r)/2)}{\cos(\alpha(r)/2)}\right]^4, \tag{7}$$

where η_0 is the wave impedance of free space, and $K(m)$ is the complete elliptic integral of the first kind [12, 20]. Next, the impedance profile obtained from Eq. (7) for r from 0 to L_A is converted to the reflected voltage in the 400Ω transmission line which feeds the TEM feed arms at the apex.

Fig. 4 shows the reflected voltage predicted from the impedance profile for a step-like pulse with $t_{10\text{-}90\%}/\tau_a = 0.1$. This reflected voltage is inverted ($-V_{refl}/V_0$) and compared with

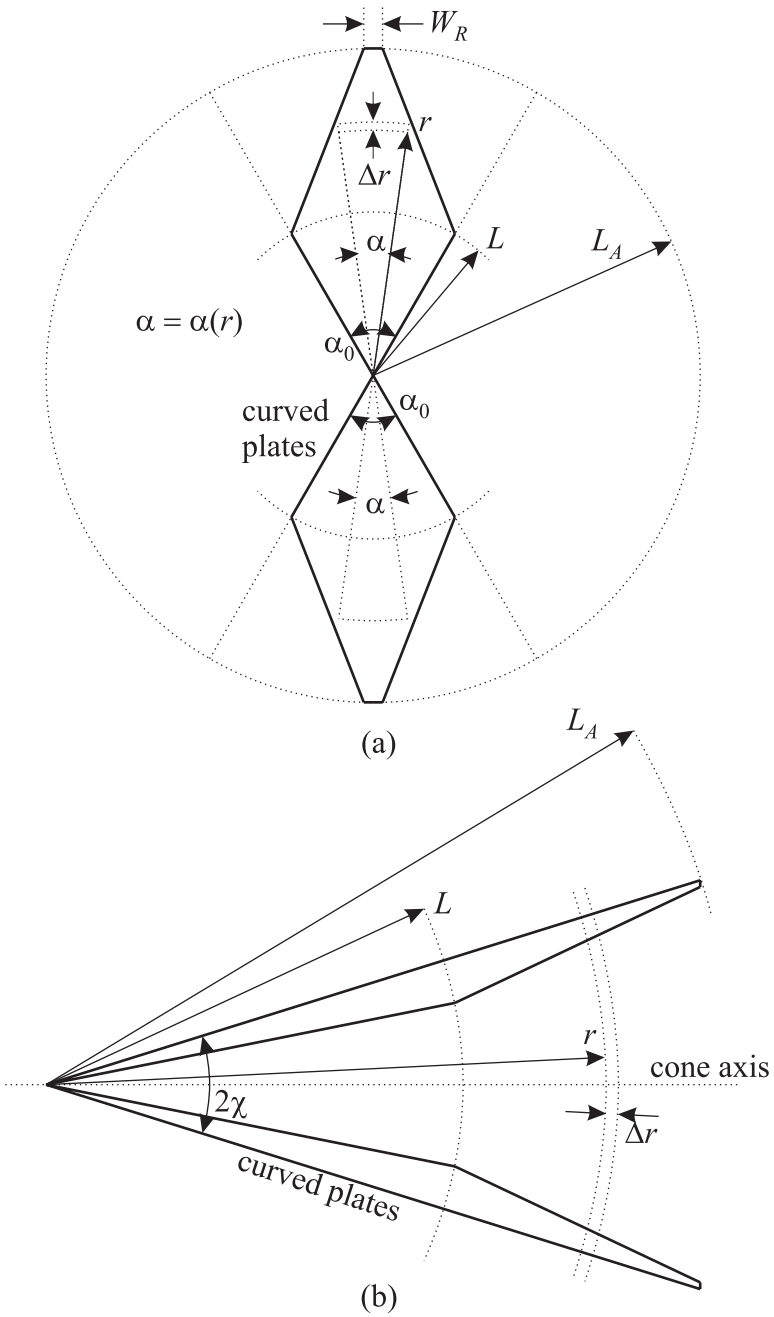

Fig. 3. Schematic of the tapered TEM feed arms. (a) Projection onto the plane normal to the cone axis. (b) Side view.

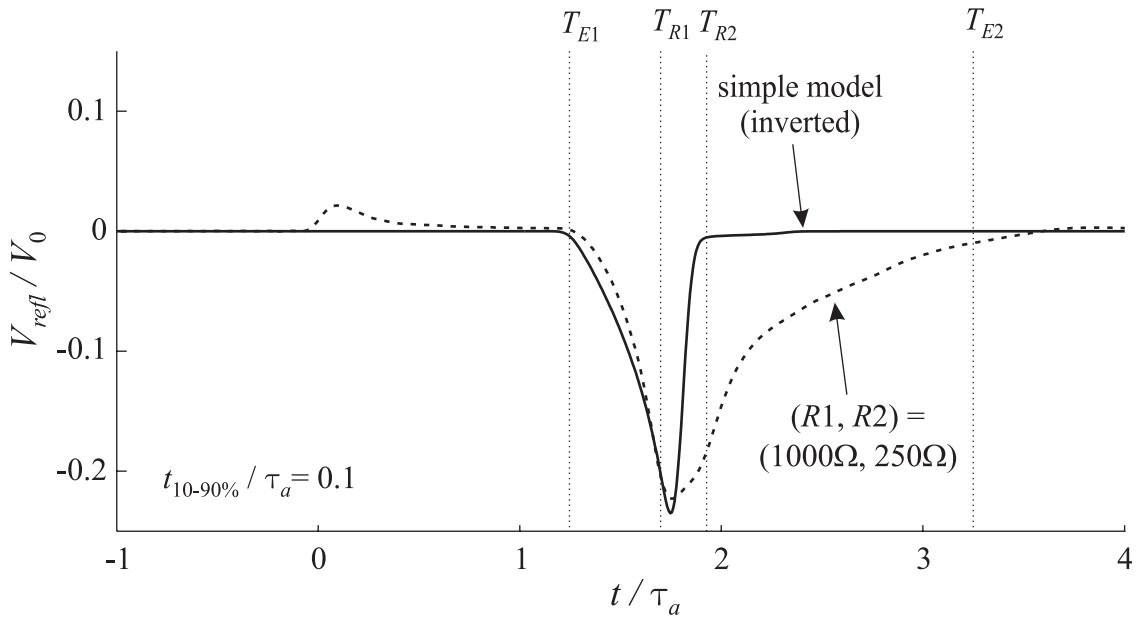

Fig. 4. Comparison of the reflected voltages. The solid line is the reflected voltage predicted by the simple model for the IRA with a tapered TEM feed arm. The dotted line is the reflected voltage predicted by the numerical model for the IRA with Model I geometry (Fig. 2).

the waveform for $(R1, R2) = (1000\Omega, 250\Omega)$ in Fig. 2. The lines are roughly on top of each other over the interval between T_{E1} and T_{R1}. This implies that the reflected signal from the taper will mostly cancel the signal over the interval between T_{E1} and T_{R1}, which will be demonstrated next by numerically modeling the IRA with these tapered TEM feed arms.

The modeling technique used in the previous section is used to model the IRA with the tapered TEM feed arms. The mesh for the lower 75 frequencies contain 5295 triangle elements, and the mesh for the higher 75 frequencies contain 10516 triangle elements. The mesh for the higher frequencies is shown in Fig. 5. The total run time for the mesh current calculation was approximately 76.1 hours on the same machines used in the previous section.

The reflected voltage for the IRA with the tapered TEM feed arms is compared with those for the three IRAs in the previous section in Fig. 2. Note that the reflected voltage is significantly lowered, and the polarity is changed. The reflection from the taper slightly overcompensates the signal from the reflector. This reflection can be further reduced by refining the shape of the arm taper [22].

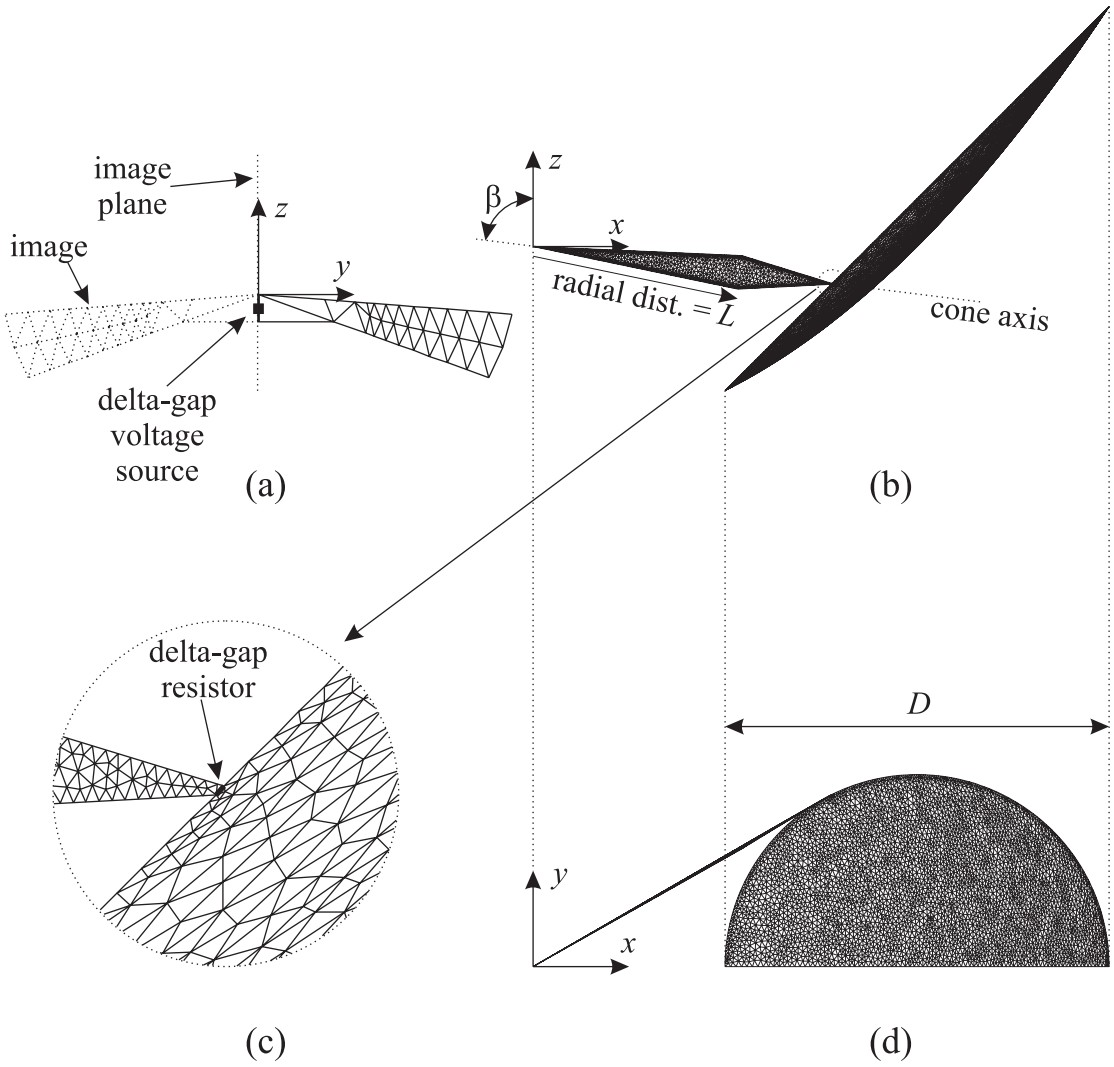

Fig. 5. Mesh for the high frequency model of the offset IRA. (a) Magnification of the region around the feed apex. (b) Projection on to x-z plane. (c) Magnification of the region around the TEM feed arm termination. (d) Projection on to x-y plane.

IV. Analysis

The taper in Eq. (5) significantly improved the performance of the IRA in terms of the reflected voltage. Thus, in this section, the IRA with the tapered TEM feed arms is further analyzed. The results is compared with those of the center-fed IRA with $F/D = 0.5$ that has been analyzed in [17]. The center-fed IRA has conical coplanar plate arms, which do not cause any blockage in the geometrical optics sense but actually cause blockage by scattering the signal from the reflector. The center-fed IRA has two pairs of 400Ω TEM

TABLE I

DIMENSIONS OF THE IRAS.

	F/D	L/D	Z_c	β	TEM feed arms
Offset IRA	0.5	0.625	400Ω	82.9°	curved
Center-fed IRA	0.5	0.5	400Ω	0°	coplanar

feed arms in [17]. Here, the number of arms is reduced to one to make fair comparisons, i.e., the same number of TEM feed arms, the same characteristic impedance of the TEM feed arms, and the same focal length to diameter ratio. The geometries of the two IRAs are summarized in Table I.

First, the reflected voltages for the two IRAs are compared in Fig. 6 for a step-like pulse with $t_{10\text{-}90\%}/\tau_a = 0.1$ and a Gaussian pulse with $t_{FWHM}/\tau_a = 0.1$ incident in a 400Ω transmission line. The reflected voltage for the offset IRA is lower than that for the center-fed IRA. Note that the TEM feed arms of both IRAs are linearly tapered in an attempt to lower the reflected voltage by allowing the signal from the taper to cancel the signal from the reflector [21]. The cancellation is seen to be more effective in the offset IRA than in the center-fed IRA.

In Fig. 7, the radiated fields on boresight for a step-like pulse with $t_{10\text{-}90\%}/\tau_a = 0.1$ are compared as functions of time $t_r = t - r/c$. The biggest difference between the two waveforms is found in the tail. The tail waveform of the offset IRA is smaller in amplitude and simpler in shape than that of the center-fed IRA. Unlike in the center-fed IRA, the TEM feed arms are mostly removed from the aperture in the offset IRA. Thus, the multiple reflections between the TEM feed arms and the reflector is small, and therefore the tail waveform is small and simple. The prepulse amplitudes are slightly different because of the difference in the TEM feed arms. The impulse amplitudes are essentially the same.

Fig. 8 shows the radiation patterns of the two IRAs. The radiated fields are plotted for a step-like pulse with $t_{10\text{-}90\%}/\tau_a = 0.1$ at a number of observation angles. Here, the y-z and x-z planes are defined as the E- and H-planes, respectively. The angles on the graphs are the angles made by the z-axis and the position vector of an observer. The sign of an

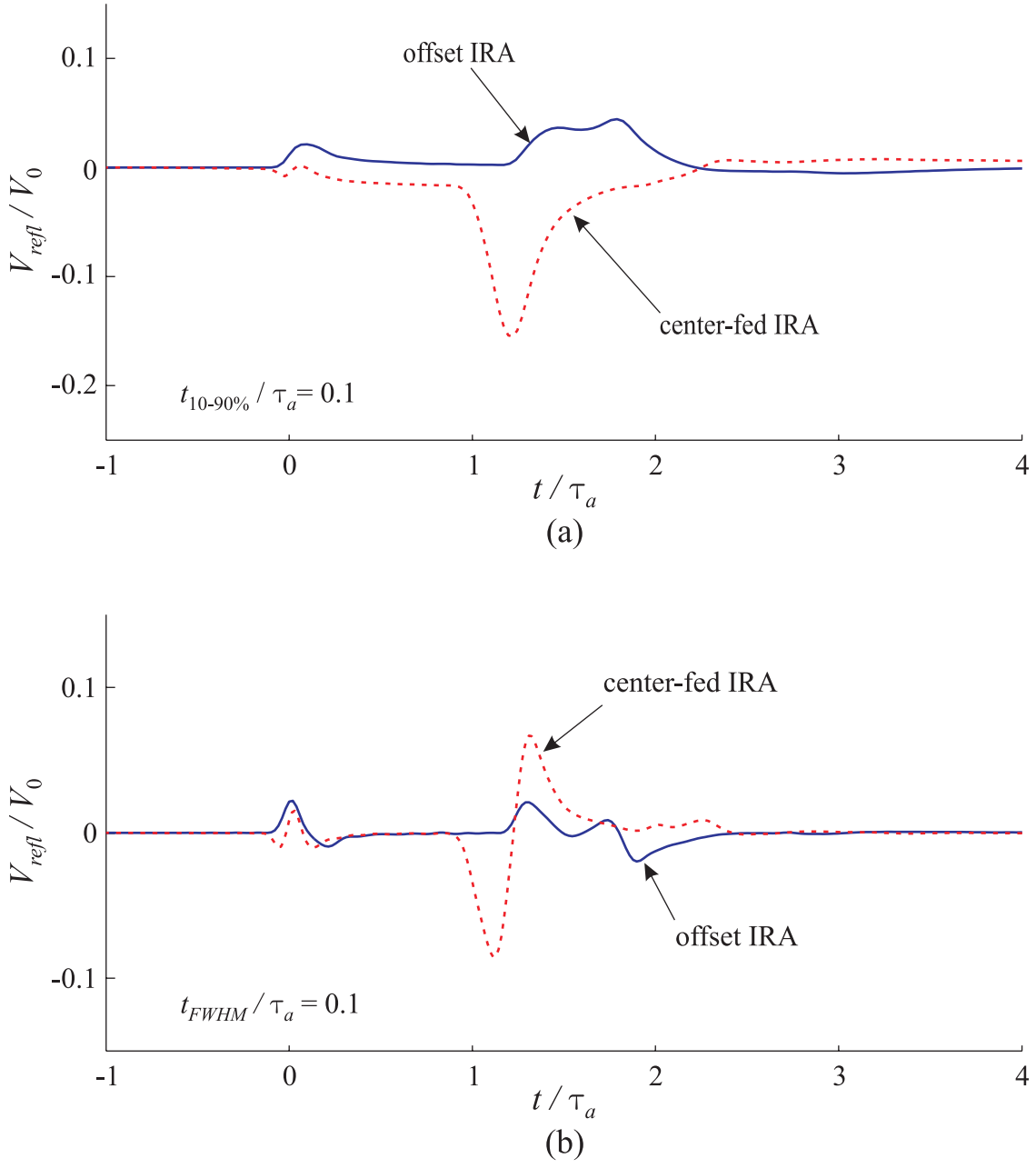

Fig. 6. Reflected voltages for the offset IRA (solid line) and center-fed IRA (dotted line). Input pulses for the graphs are (a) a step-like with $t_{10\text{-}90\%}/\tau_a = 0.1$ and (b) a Gaussian with $t_{FWHM}/\tau_a = 0.1$.

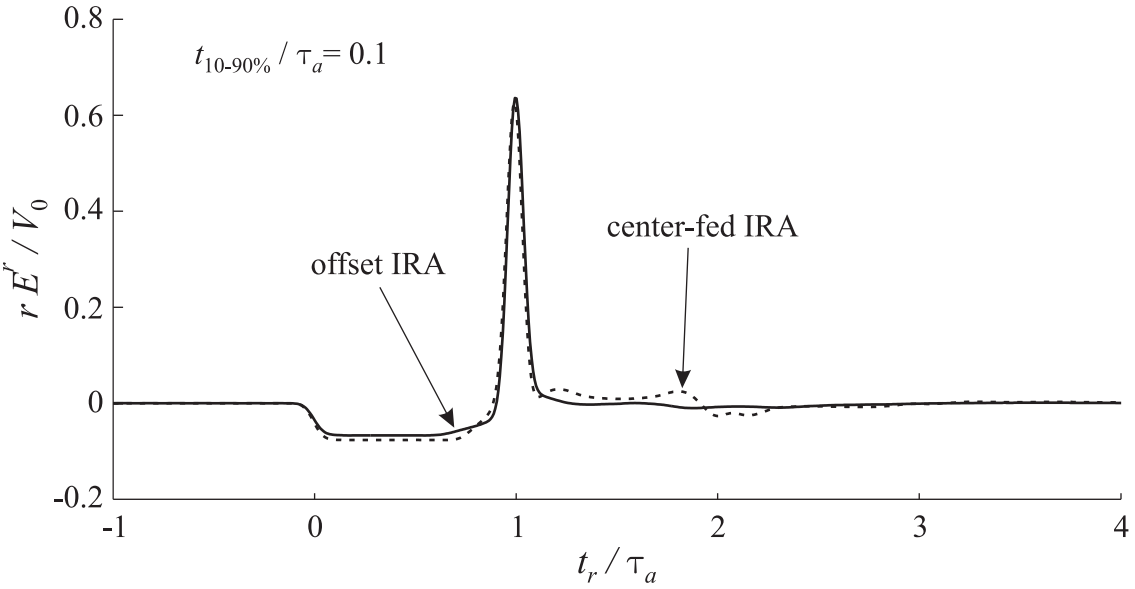

Fig. 7. Radiated fields from the offset IRA and the center-fed IRA on boresight. The input pulse for this graph is a step-like with $t_{10\text{-}90\%}/\tau_a = 0.1$.

angle coincides with the sign of the observer's x- or y-coordinate.

The radiation patterns of the center-fed IRA are symmetric about the 0° angle both in the E- and H-planes because the geometry of the antenna is symmetric with respect to the z-axis. The radiation pattern of the offset IRA is symmetric about the 0° angle in the E-plane. However, it is asymmetric in the H-plane because the geometry of the offset IRA is symmetric only across the E-plane.

Note that the radiated fields are seen to be minimal around 90° for the offset IRA and 180° for the center-fed IRA. The reason for this is that the reflectors shadow the observers in the directions of 82.9° for the offset IRA and 180° for the center-fed IRA. This phenomenon may be useful in certain applications, such as bistatic radar systems where the antennas are placed side by side looking in the same direction (Fig. 9). In such a case, the coupling between the antennas can be reduced significantly by placing two offset IRAs in the shadows of each other.

Fig. 10 shows the prepulse and impulse amplitude distributions as functions of observation angle for a number of step-like pulses. Because the impulse and prepulse are not clearly defined off boresight, simply the maximum and minimum of the radiated field

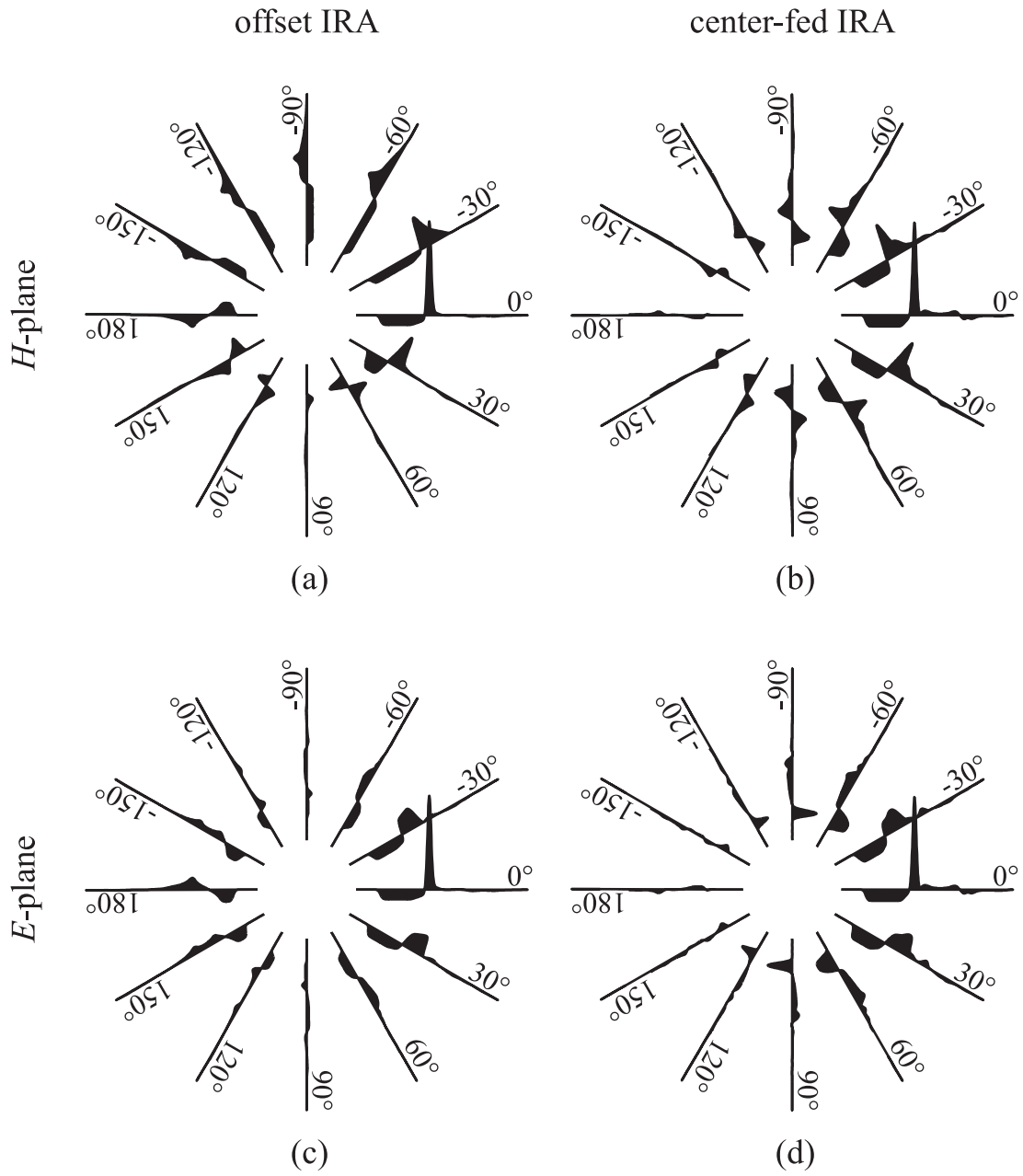

Fig. 8. Radiated fields of the offset IRA and the center-fed IRA for a step-like pulse with $t_{10\text{-}90\%}/\tau_a = 0.1$. (a), (b) Radiated fields in the H-plane. (c), (d) Radiated fields in the E-plane.

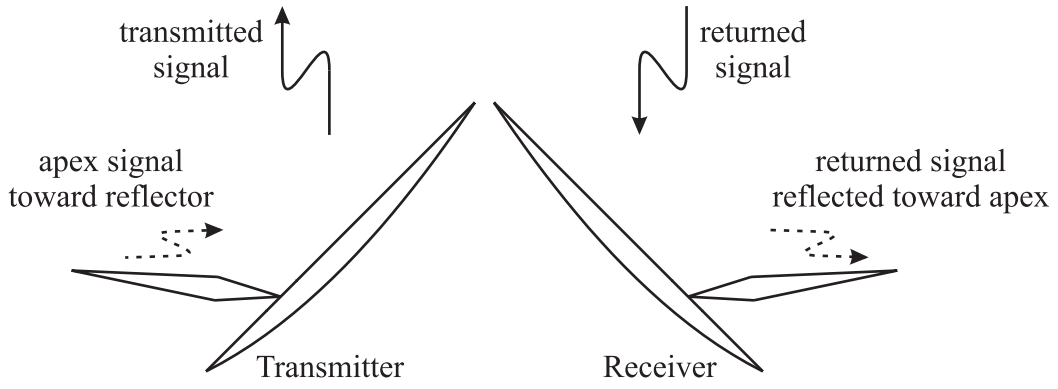

Fig. 9. Suggested configuration for bistatic radar systems. The transmitter sends out a signal toward a target, and the receiver receives the reflected signal from the target. Because the antennas are in the shadow of each other the coupling between the antennas is expected to be low.

(rE^r/V_0) are taken as the impulse and prepulse amplitudes and plotted above and below zero, respectively. The full-angular-width half-maximum (θ_{FWHM}), which is the angular width between the two observation angles in a plane where the amplitude drops by half from its maximum, decreases with decreasing pulse rise time for both IRAs. Thus, the impulse becomes more directive for both IRAs with decreasing pulse rise time. Note the asymmetric pattern of the offset IRA in the H-plane. The asymmetric pattern is more apparent in the prepulse amplitude distribution than in the impulse amplitude distribution.

The impulse amplitude of the offset IRA is slightly lower than that of the center-fed IRA at large angles. However, at small angles, the impulse amplitude distributions for both IRAs are almost the same. The impulse of the offset IRA is slightly larger than that of the center-fed IRA on boresight (0.637 vs. 0.626 for $t_{10\text{-}90\%}/\tau_a = 0.1$). For a fast rising pulse, the θ_{FWHM} of the offset IRA is slightly larger in the E-plane (25.8° vs. 24.4° for $t_{10\text{-}90\%}/\tau_a = 0.1$) and slightly smaller in the H-plane (36.5° vs. 37.2° for $t_{10\text{-}90\%}/\tau_a = 0.1$). These slight differences are negligible for most practical applications.

Next, the electric fields at distances close to the antenna are discussed. For convenience of the analysis, the coordinate origin is redefined. In Fig. 11, the new coordinate origins for the antennas are shown. For each antenna, a plane that is normal to the z-axis and passes through the point on the antenna with the largest z-coordinate is taken. The coordinate origin is located at the center of the disc formed by the projection of the reflector onto the plane. The distance from the new coordinate origin to an observer is designated as

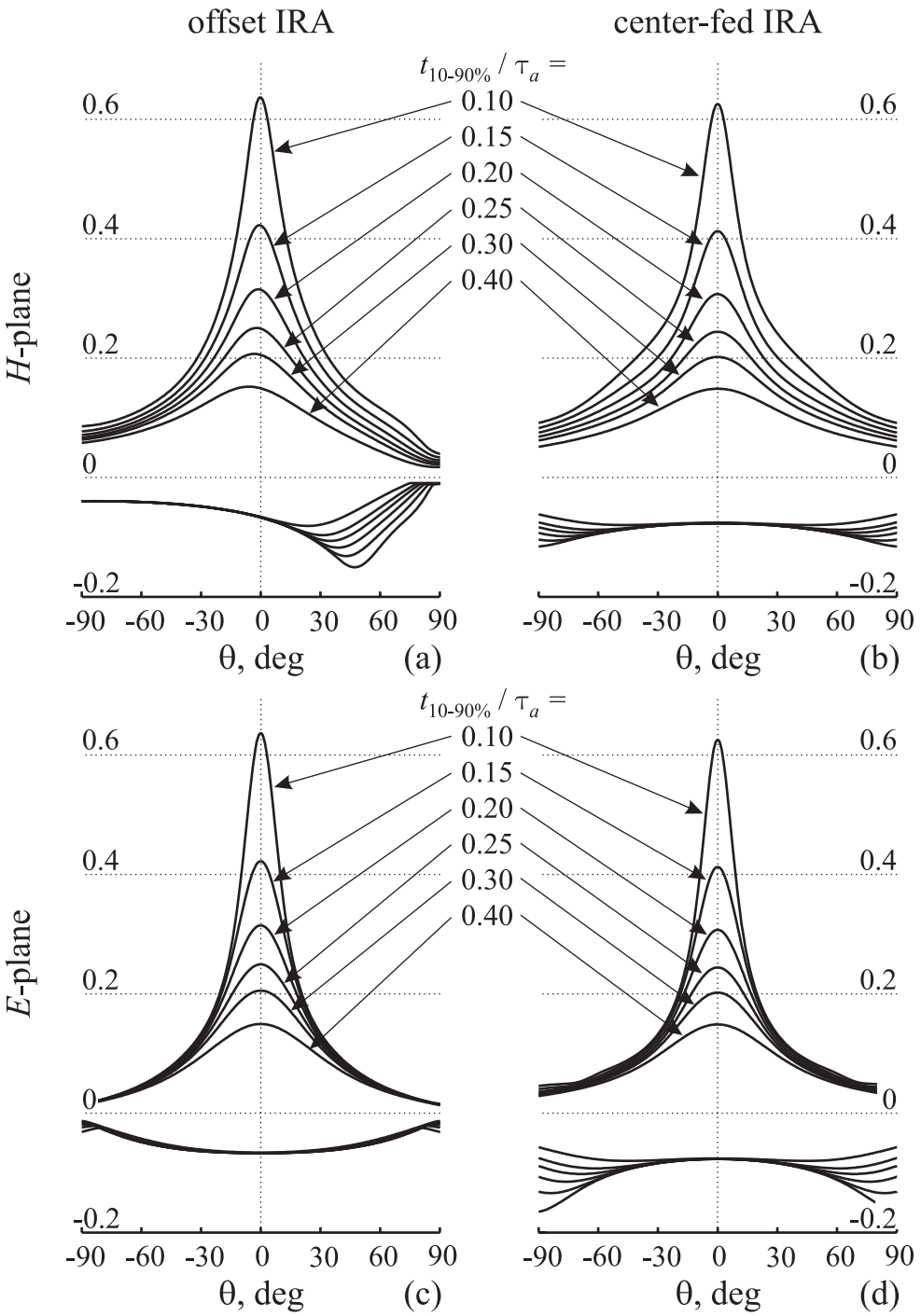

Fig. 10. Impulse amplitude (maximum of rE^r/V_0) and prepulse amplitude (minimum of rE^r/V_0) at a range of observation angle for a number of step-like pulses. The lines above zero represent the impulse amplitudes and the lines below zero represent the prepulse amplitudes. The lines that are farther from zero are those for smaller rise times. (a), (b) Amplitudes in the H-plane. (c), (d) Amplitudes in the E-plane.

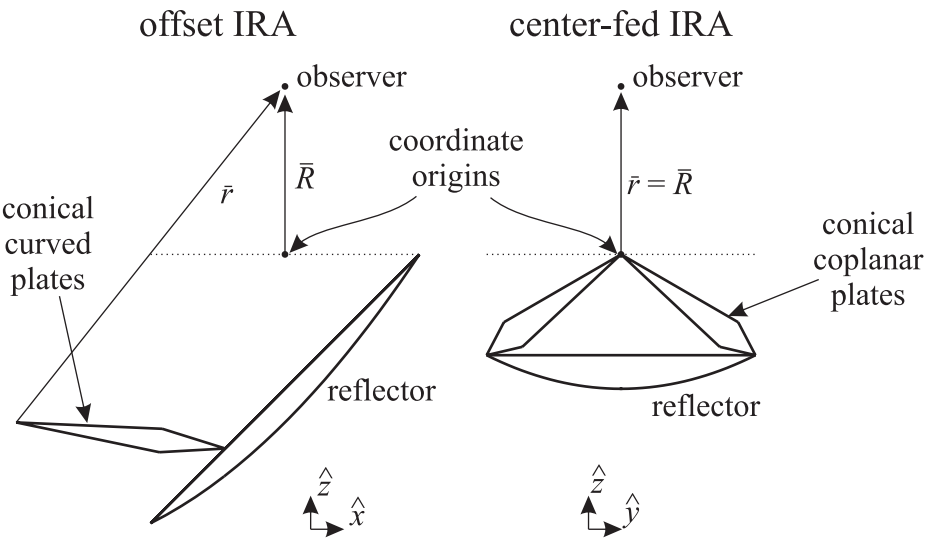

Fig. 11. New coordinate origins for the offset IRA and the center-fed IRA. $r = |\bar{r}|$ is the distance from the apex to the observer. $R = |\bar{R}|$ is the distance from the new coordinate origin to the observer.

$R = |\bar{R}|$, and the distance from the old coordinate origin (apex of the TEM feed arms) to the observer is designated as $r = |\bar{r}|$. For the center-fed IRA, R and r are the same.

Fig. 12 shows the electric field waveforms of the two IRAs at a number of points along the new z-axis. In each graph, the electric field (RE_y/V_0) is plotted for a step-like pulse with $t_{10\text{-}90\%}/\tau_a = 0.1$ and vertically displaced according to the observation distance R. Each of the graphs is for the retarded time $t_r = t - r/c$ so the waveforms are all aligned at $t_r/\tau_a = 0$ at which the first signal from the antenna is seen by the observer.[2] The figure shows the development of the impulse for both IRAs as the observer moves out.

In Fig. 12 (a), the impulse appears earlier than $t_r/\tau_a = 1$ and gets closer to $t_r/\tau_a = 1$ as the observer moves out. The dominant reason for this is that the path length difference $r - R$ is not constant as R is varied. This difference converges to $2F$ for large values of R, and the impulse appears at $t_r/\tau_a = 1$ in the far zone. It is less than $2F$ for finite values of R, and the impulse appears earlier than $t_r/\tau_a = 1$ in the near zone. Note that in Fig. 12 (a), the prepulse amplitude varies slightly because the observation angle varies with respect to the cone axis as the observer moves out.

[2]Note that time is retarded by r/c and not by R/c.

In Fig. 12 (b), the impulse appears later than $t_r/\tau_a = 1$ and gets closer to $t_r/\tau_a = 1$ as the observer moves out. This can be viewed as a diffraction problem. The impulse is formed by the superposition of the aperture surface signal (leading edge of the impulse; geometrical optics signal) and the aperture edge signal (trailing edge of the impulse; diffracted signal) [13,23]. The aperture surface signal always arrives at an observation point at $t_r/\tau_a = 1$. The aperture edge signal arrives at the observation point later than $t_r/\tau_a = 1$. As the observer moves out, the interval of the two signals converges to zero. Thus, at distances close to the antenna, the impulse is fat, and the peak appears later than $t_r/\tau_a = 1$.

Fig. 13 shows the spot sizes of the two IRAs in the E- and H-planes. To determine a spot size, an imaginary observation plane that is normal to the z-axis is placed at a distance, where the impulse amplitude (maximum of E_y) distribution is recorded. Then the full-width half-maximum of the distribution is taken as the spot size. In Fig. 13, half-maximum points are plotted as functions of the z-coordinate of the observation plane. Thus, the distance between a pair of lines at a z-coordinate is the spot size at the observation plane. The input pulses for the figure are three step-like pulses with $t_{10\text{-}90\%}/\tau_a = 0.1$, 0.15, and 0.2. The solid lines are the half-maximum points for the offset IRA and the dotted lines are those for the center-fed IRA. The lines that are closer to $x = 0$ or $y = 0$ are those for the pulses with smaller $t_{10\text{-}90\%}$. In Fig. 13 (a), the spots for the offset IRA are seen to be asymmetrical due to the asymmetry in the geometry. Note that the spot sizes for fast rising pulses are just slightly different. The spot size of the offset IRA is slightly larger in the E-plane and slightly smaller in the H-plane than the center-fed IRA.

Finally, the power budgets for the two IRAs are compared in Fig. 14. The power reflected back in the transmission line (P_{refl}), the power dissipated in the resistors (P_{diss}), and the power radiated in free space (P_{rad}) are shown as functions of normalized frequency (D/λ). At most frequencies, the center-fed IRA radiates more power and dissipates less power than the offset IRA, and therefore the center-fed IRA has higher radiation efficiency. However, Fig. 10 showed that the impulse amplitude of the offset IRA is slightly larger and θ_{FWHM}'s of the two antennas are very close. This implies that the offset IRA radiates roughly as much power through the impulse radiation around the boresight direction as the

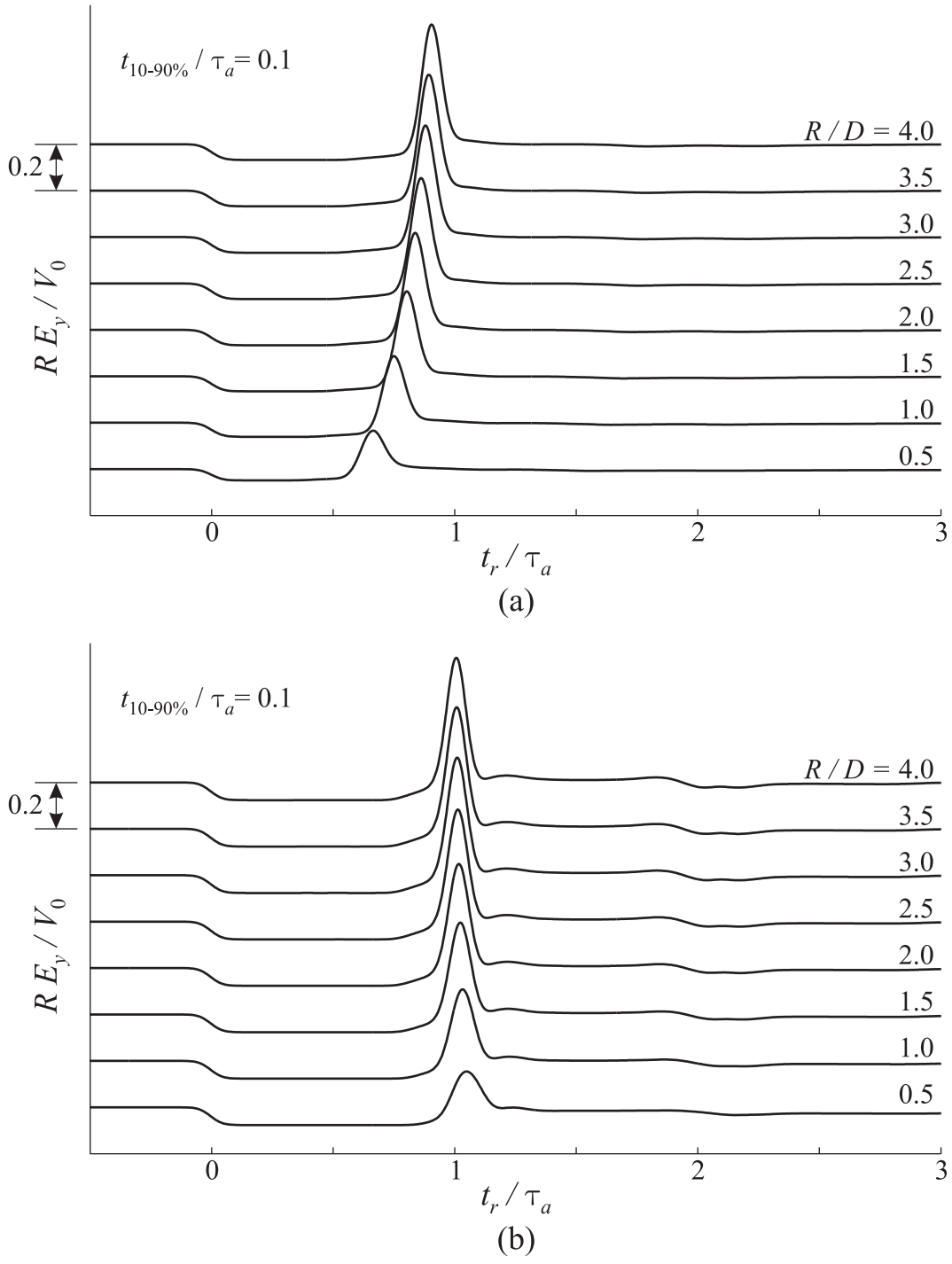

Fig. 12. Near field waveforms from (a) the offset IRA and (b) the center-fed IRA for a step-like pulse with $t_{10\text{-}90\%}/\tau_a = 0.1$.

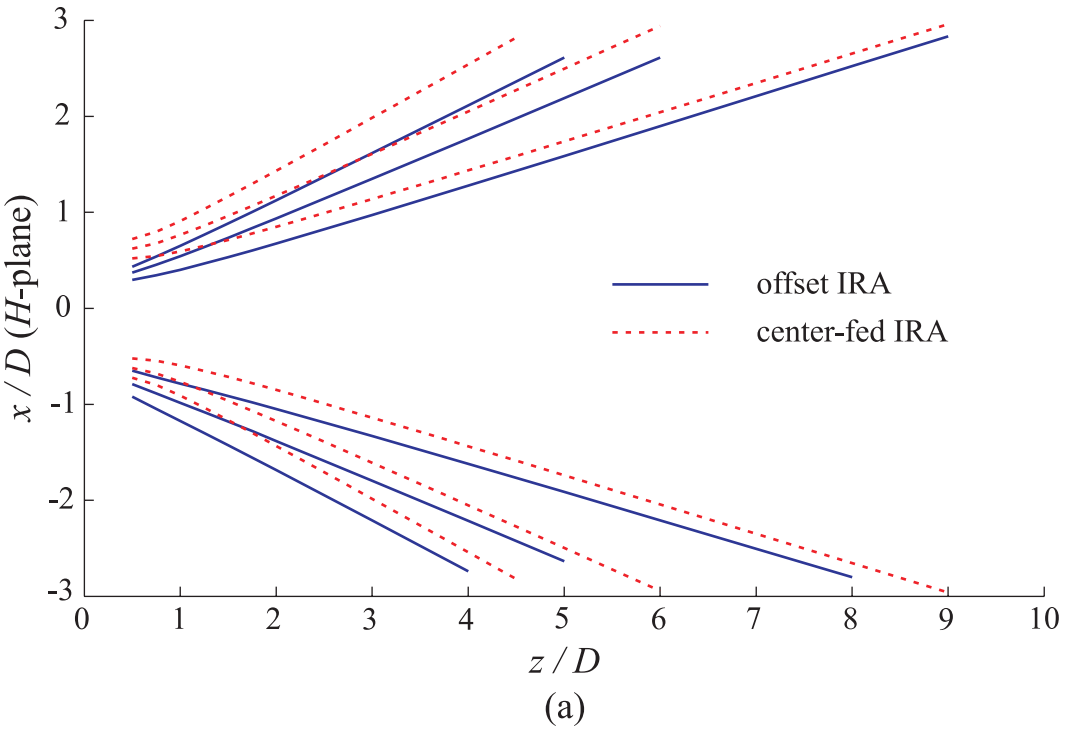

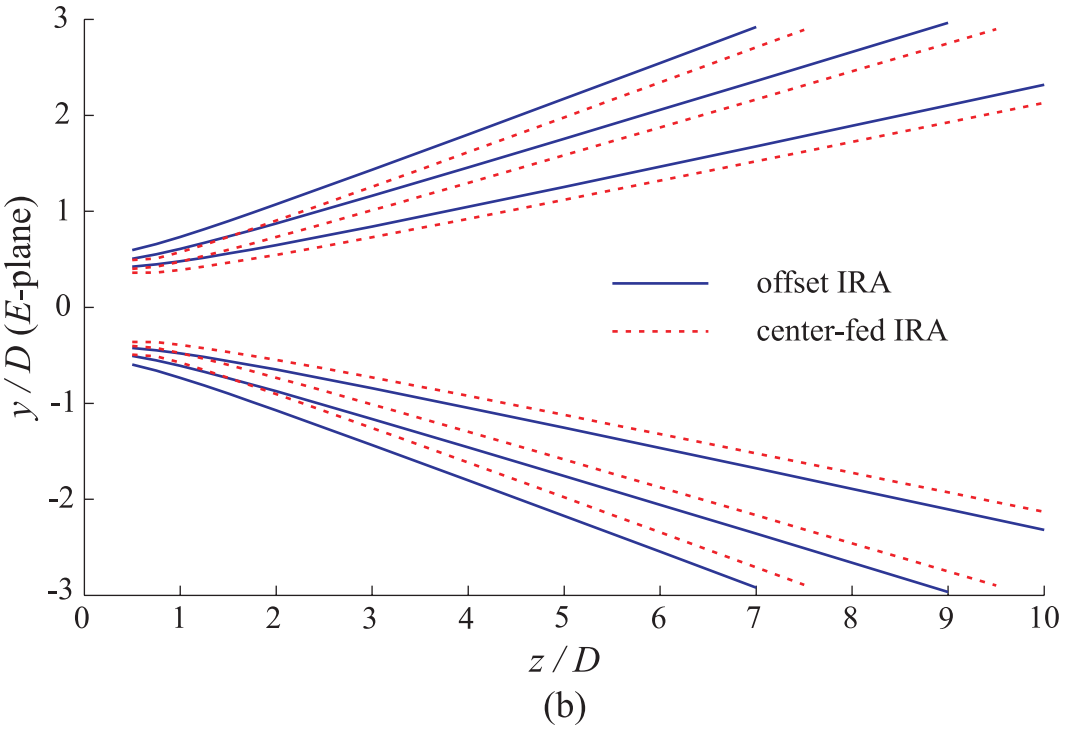

Fig. 13. Spot sizes (a) in the H-plane and (b) in the E-plane. The input pulses are step-like with $t_{10\text{-}90\%}/\tau_a =$ 0.1, 0.15, and 0.2 for the lines from inside.

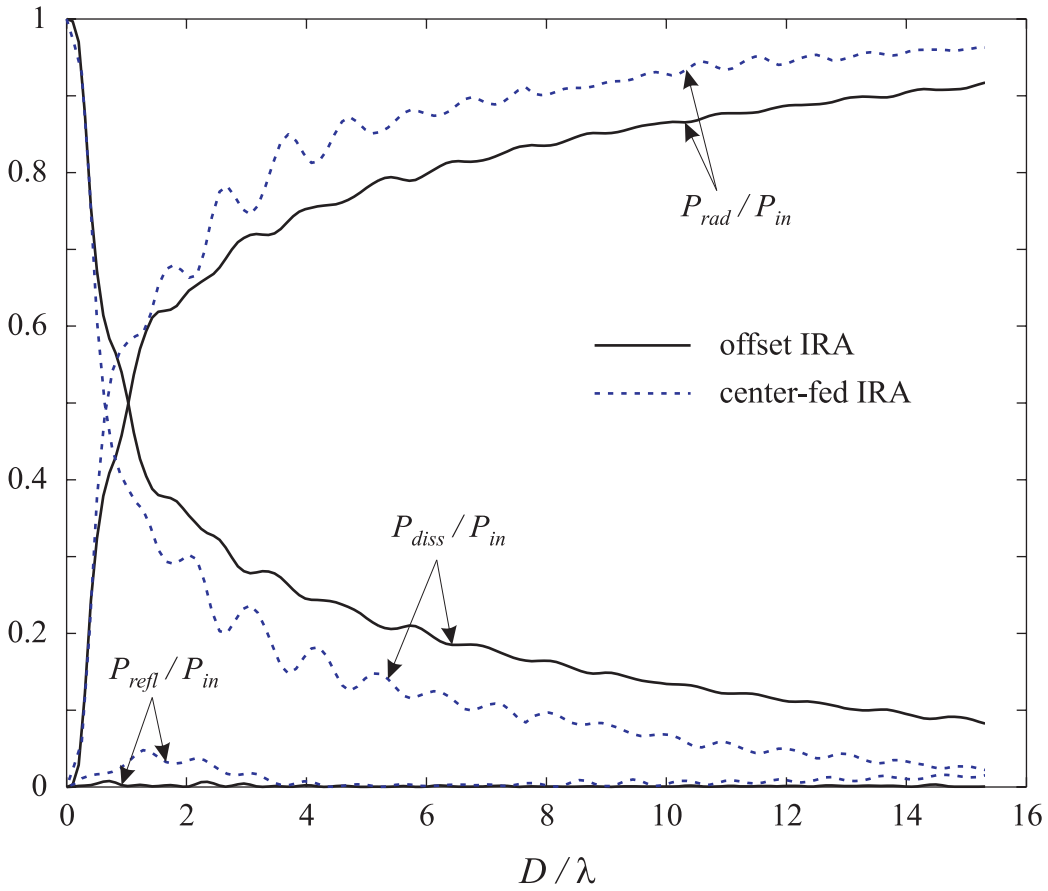

Fig. 14. Comparison of the power budgets for the offset IRA (solid line) and the center-fed IRA (dotted line) as functions of normalized frequency (D/λ).

center-fed IRA does even though the total radiated power for the offset IRA is smaller than that for the center-fed IRA. This is a desired characteristic in many applications, such as ultra-wideband weapons and remote sensing.

V. Conclusion

The tail waveform of the offset IRA was significantly lower in amplitude and simpler in shape than that of the center-fed IRA. The reason for this was that the multiple reflections between the TEM feed arms and the reflector were mostly removed in the offset IRA geometry.

For both antennas, the radiation was small behind the reflector. This property of the offset IRA can be useful in bistatic radar applications where the antennas are placed side by side looking in the same direction because the coupling between the antennas can be reduced significantly. The offset IRA can also be effective as a near field sensor, such as a ground-penetrating radar, because the reflector does not reflect the signal from the ground back toward the ground, and thus the multiple reflections between the antenna and the ground can be reduced.

The impulse amplitudes on boresight and the impulse beam widths for the two antennas were essentially the same. However, the total radiated power was smaller for the offset IRA than it was for the center-fed IRA. This is a desired characteristic because the offset IRA will cause less electromagnetic interference in the nearby equipment while radiating as much power through impulse radiation around boresight as the center-fed IRA does.

Note that one advantage of the center-fed IRA is that one can add a second pair of TEM feed arms to the center-fed IRA to lower the input impedance [17, 24]. The offset IRA geometry does not allow the second pair of TEM feed arms so it will be more difficult to match the offset IRA to the source because of its higher impedance.

Different types of TEM feed arms are worth investigating for use in the offset IRA geometry. One candidate may be conical flat plates [19]. The flat plates can be attached at the rim of the reflector or on the surface of the reflector. In the latter case, the aperture shape will be different from a circle, and one may remove the part of the reflector beyond the flat plates.

There still remains a question of how to run the physical transmission line to feed the offset IRA. One choice is to run the transmission line from the edge of the reflector ($E1$) to the apex [24]. In this geometry, the transmission line should minimally interfere with the prepulse and the impulse. This geometry can easily built into the offset IRA geometry because one way to build the TEM feed arms is to print them on a thin flexible dielectric substrate and then fold the substrate into a cone shape. In this case, the transmission line can also be printed on the substrate. A second choice is to run the transmission line through a hole on the reflector to the apex along the rotational axis of the cone. In this geometry, the

transmission line should not disturb the spherical TEM wave toward the reflector; however, the reflector scattered wave will be disturbed by the transmission line. A third choice is to run the transmission line along the TEM feed arms. In this geometry, the transmission line hides behind the TEM feed arms, so as not to disturb the radiated field. However, this geometry requires extra circuits to avoid interfering with the TEM feed arm terminations.

VI. Acknowledgement

This work is supported in part by the US Army CECOM RDEC Night Vision and Electronic Sensors Directorate, Countermine Division.

References

1. G. Sower, J. Eberly, and E. Christy, "GSTAMIDS ground-penetrating radar: hardware description," in *Detection and Remediation Technologies for Mines and Minelike Targets VI, Proc. SPIE*, vol. 4394, Apr. 2001, pp. 651–661.

2. E. G. Farr and L. H. Bowen, "Impulse radiating antennas for mine detection," in *Detection and Remediation Technologies for Mines and Minelike Targets VI, Proc. SPIE*, vol. 4394, Apr. 2001, pp. 680–691.

3. J. R. R. Pressley, D. Pabst, G. Sower, L. Nee, B. Green, and P. Howard, "Ground standoff mine detection system (GSTAMIDS) engineering, manufacturing and development (EMD) block 0," in *Detection and Remediation Technologies for Mines and Minelike Targets VI, Proc. SPIE*, vol. 4394, Apr. 2001, pp. 1190–1200.

4. T. P. Montoya, "Vee dipole antennas for use in short-pulse ground-penetrating radars," Ph.D. dissertation, Georgia Institute of Technology, Mar. 1998.

5. F. M. Tesche, "Some considerations for the design of pulse-radiating antennas," Sensor and Simulation Notes #398, Jul. 12, 1996.

6. C. E. Baum and E. G. Farr, "Impulse radiating antennas," in *Ultra-Wideband, Short Pulse Electromagnetics*. H. Bertoni *et al.,* Eds. New York: Plenum, 1993, pp. 139–147.

7. E. G. Farr, C. E. Baum, and C. J. Buchenauer, "Impulse radiating antennas, part II," in *Ultra-Wideband, Short Pulse Electromagnetics 2*. L. Carin and L. B. Felsen, Eds. New York: Plenum, 1995, pp. 159–170.

8. D. V. Giri, H. Lackner, I. D. Smith, D. W. Morton, C. E. Baum, J. R. Marek, W. D. Prather, and D. W. Scholfield, "Design, fabrication, and testing of a paraboloidal reflector antenna and pulser system for impulse-like waveforms," *IEEE Trans. Plasma Sci.*, vol. 25, no. 2, pp. 318–326, Apr. 1997.

9. C. E. Baum, E. G. Farr, and D. V. Giri, "Review of impulse-radiating antennas," in *Reviw of Radio Science 1996-1999*. W. R. Stone, Ed. Oxford University Press, 1999, ch. 16, pp. 403–439.

10. Y. Rahmat-Samii, "Analysis of blockage effects on TEM-fed paraboloidal reflector antennas," Sensor and Simulation Notes #347, Oct. 25, 1992.

11. Y. Rahmat-Samii and D. W. Duan, "Axial feed of a TEM-fed UWB reflector antenna: The PO/PTD construction," Sensor and Simulation Notes #363, Dec. 16, 1993.

12. E. G. Farr, "Optimizing the feed impedance of impulse radiating antennas, Part I: Reflector IRAs," Sensor and Simulation Notes #354, Jan. 1993.

13. C. E. Baum, "Radiation of impulse-like transient fields," Sensor and Simulation Notes #321, Nov. 25, 1989.

14. ——, "Variations on the impulse-radiating antenna theme," Sensor and Simulation Notes #378, Feb. 10, 1995.

15. R. M. Sharpe, J. B. Grant, N. J. Champagne, W. A. Johnson, R. E. Jorgenson, D. R. Wilton, W. J. Brown, and J. W. Rockway, "EIGER: Electromagnetic interactions generalized," in *IEEE AP-S Int'l Symp. Digest, Quebec, Canada*, Jul. 1997, pp. 2366–2369.

16. Lawrence Livermore National Laboratory. (2001, March 5) EIGER - A Revolution in Computational Electromagnetics. [Online]. Available: http://cce.llnl.gov/eiger/

17. K. Kim and W. R. Scott, "Numerical analysis of the impulse-radiating antenna," Sensor and Simulation Notes #474, June 3, 2003.

18. V. Jamnejad-Dailami and Y. Rahmat-Samii, "Some important geometrical features of conic-section-generated offset reflector antennas," *IEEE Trans. Antennas Propagat.*, vol. AP-28, no. 6, pp. 952–957, Nov. 1980.

19. E. G. Farr, "Optimization of the feed impedance of impulse radiating antennas. Part II: TEM horns and lens IRAs," Sensor and Simulation Notes #384, Nov. 1995.

20. M. Abramowitz and I. A. Stegun, *Handbook of Mathematical Functions with Formulas, Graphs, and Mathematical Tables.* New York: Dover, 1972.

21. C. E. Baum, "Some topics concerning feed arms of reflector IRAs," Sensor and Simulation Notes #414, Oct. 31, 1997.

22. K. Kim, "Numerical and experimental investigation of impulse-radiating antennas for use in sensing applications," Ph.D. dissertation, Georgia Institute of Technology, April 2003.

23. G. S. Smith, *An Introduction to Classical Electromagnetic Radiation.* Cambridge, UK: Cambridge University Press, 1997, ch. 4.

24. C. E. Baum, "Configuration of TEM feed for an IRA," Sensor and Simulation Notes #327, Apr. 27, 1991.